Chemical Engineering Journal xxx (xxxx) 130713

Contents lists available at ScienceDirect

Chemical Engineering Journal

journal homepage: www.elsevier.com/locate/cej

Lithium recovery from hydraulic fracturing flowback and produced water using a selective ion exchange sorbent

Adam Seip [a], Salman Safari [a], David M. Pickup [b], Alan V. Chadwick [b], Silvia Ramos [b], Carmen A. Velasco [c, d], José M. Cerrato [c], Daniel S. Alessi [a, *]

[a] Department of Earth and Atmospheric Sciences, University of Alberta, Edmonton, Alberta T6G 2E3, Canada
[b] School of Physical Sciences, University of Kent, Canterbury, Kent CT2 7NH, UK
[c] Department of Civil Engineering, University of New Mexico, Albuquerque, NM 87131, United States
[d] Department of Chemical Engineering, Universidad Central del Ecuador, Ritter s/n & Bolivia, Quito 17-01-3972, Ecuador

ARTICLE INFO

Keywords:
Lithium
Hydraulic fracturing
Hydrometallurgy
Nanoparticles
Ion exchange
Reductive dissolution

ABSTRACT

Increased demand for lithium products for use in lithium-ion batteries has led to a search for new lithium resources in recent years to meet projected future consumption. One potential lithium resource is low lithium bearing brines that are discharged from hydraulically fractured oil and gas wells as flowback and produced water (FPW). In this way, hydraulic fracturing presents an opportunity to turn what is normally considered wastewater into a lithium resource. In this research, two manganese-based lithium-selective adsorbents were prepared using a co-precipitation method and were employed for lithium recovery from FPW. At optimized conditions, lithium uptake reached 18 mg g^{-1}, with a > 80% lithium recovery within 30 min. The recovered lithium was isolated and concentrated to 15 mM in an acidic final product. The degree of sorbent loss during acid desorption of lithium was significantly higher for sorbents used in the FPW as compared to recovery from a synthetic lithium-bearing brine (4.5% versus 0.8%). Thus, we propose that organic molecules present in the FPW reduce manganese in the sorbent structure during lithium sorption, leading to increased sorbent loss through reductive dissolution. Systematic characterization including wet chemical manganese valence measurements, along with EXAFS, XPS, and TEM-EELS show that exposure to FPW causes tetravalent manganese in the bulk sorbent structure to be reduced during lithium sorption, and subsequently dissolves during acid desorption. Partial removal of these organic molecules by nanofiltration leads to decreased sorbent dissolution in acid. In this way, we show that dissolved organic molecules represent a critical control on the reductive dissolution of manganese-based lithium ion exchange sorbents. This research provides some promising results on the use of manganese-based lithium sorbents in FPW.

1. Introduction

Lithium products represent a valuable resource for the rapidly growing electric vehicle industry [1–3]. Global lithium production increased by an estimated 113% between 2016 and 2018, with 56% of 2018 lithium end-use going toward lithium based battery production [4]. It is anticipated that this trend will continue, and that lithium availability may become the rate limiting factor in lithium battery production in the future [5]. Currently, almost all of the lithium products used in industry in North America are imported [6]; for this reason, lithium supply security has become a priority for technology companies in the United States [4]. One potential lithium reserve that exists in North America is

Abbreviations: FPW, Hydraulic Fracturing Flowback and Produced Water; EXAFS, Extended X-Ray Absorption Fine Structure; XPS, X-Ray Photoelectron Spectroscopy; TEM-EELS, Transmission Electron Microscopy – Electron Energy Loss Spectroscopy; TDS, Total Dissolved Solids; ICP-MS/MS, Inductively Coupled Plasma – Mass Spectrometer; FTIR, Fourier-Transform Infrared Spectroscopy; TGA, Thermogravimetric Analysis; XRD, X-Ray Diffraction; XAS, X-Ray Absorption Spectroscopy; XANES, X-Ray Absorption Near Edge Structure; X-FEG, Extreme Field Emission Gun; CMOS, Complementary Metal Oxide Semiconductor; TEM, Transmission Electron Spectroscopy; BET, Brunauer-Emmett-Teller Surface Area; NPOC, Non-Purgeable Organic Carbon; TIC, Total Inorganic Carbon; NDIR, Non-Dispersive Infrared; LMO-2, Calcined Sorbent, Li:Mn Synthesis Ratio 2; HMO-2, Protonated Sorbent, Li:Mn Synthesis Ratio 2; LMO-3, Calcined Sorbent, Li:Mn Synthesis Ratio 3; HMO-3, Protonated Sorbent, Li:Mn Synthesis Ratio 3

* Corresponding author.
E-mail address: alessi@ualberta.ca (D.S. Alessi).

https://doi.org/10.1016/j.cej.2021.130713
Received 21 March 2021; Received in revised form 1 June 2021; Accepted 4 June 2021

hydraulic fracturing flowback and produced water (FPW), which would help to meet the issues of both rising global demands and lithium supply security [7,8]. FPW is a waste by-product of the hydrocarbon extraction industry [9–11]. During the fracturing process, fracturing fluid, which consists of water, sand and fracturing additives, is injected into a target geologic formation in order to fracture the rock, increase its permeability, and promote the flow of hydrocarbons toward the wellbore [10,11]. During this process, the fracturing fluid interacts with the geologic formation, interstitial water, and hydrocarbons, and a fraction of the resulting fluid returns to the surface as FPW [9,11]. The formation water in hydraulic fracturing plays is often highly saline, typically in excess of 100,000 ppm of total dissolved solids (TDS) [11], and bears lithium, in some cases in excess of 100 ppm [7]. Consequently, hydraulic fracturing supplies a mechanism of delivering lithium-bearing petroleum brine to the surface, and therefore provides an opportunity for lithium recovery.

Common methods for lithium recovery from brine include solvent extraction, electrochemistry, solar evaporation and ion exchange [12]. Many of these methods have drawbacks; both solvent extraction and the electrochemical method are not suitable for lithium extraction when concentrations of divalent cations in the brine are high [13,14], while the solar evaporation method used in South America requires a dry climate, ample sunlight, high lithium concentrations, and a long evaporation time of 1–2 years [1]. None of these methods would therefore be applicable to extraction of lithium from FPW. For these reasons, ion exchange is among the most promising technologies for use in low lithium-bearing brines such as FPW [15].

Selective ion exchange adsorbents used for lithium recovery include both manganese based and titanium based materials [16]. Spinel manganese based ion exchange sorbents represent one of the most promising lithium recovery technologies from low lithium bearing brines due to their high selectivity toward lithium and their high lithium uptake [17]. These materials have displayed the highest lithium uptake in literature of an inorganic sorbent, with reported experimental lithium uptake capacities in excess of 40 mg g^{-1} [18]. The primary challenge in commercialization of these manganese based ion exchange materials has been sorbent loss during lithium desorption in acid [19]. Identifying major parameters which affect sorbent loss and investigating potential mitigation strategies for application in FPW is therefore critical to the economic use of these sorbents.

To the best of our knowledge, there are no studies that utilize a manganese-based sorbent for lithium recovery from FPW. Jang *et al.*, [8] employed a titanium-based sorbent to recover lithium from a synthetic FPW; however, there are no extant studies that investigate lithium extraction from real field-collected FPW using an ion exchange sorbent. It is therefore not understood how the complex organic profile, which is present in the FPW due to both fracturing additives and organics indigenous to the fractured hydrocarbon-bearing formation [20], affects this lithium recovery technology. The primary objectives of this study, therefore, were to evaluate the lithium recovery performance and the chemical stability of manganese-based sorbents when used for lithium recovery from FPW.

In this study, we prepared two manganese-based sorbents at different synthesis conditions using a co-precipitation method and performed a comprehensive analysis of their physical and chemical properties in order to determine the effect of synthesis conditions on sorbent structure. The sorbents were then used to recover lithium from a sample of field collected FPW originating from the Duvernay Formation in Alberta, Canada. The performance of each sorbent in the field collected FPW was then compared to that of a synthetic FPW. Samples of each sorbent were analyzed at each point of the lithium recovery cycle from both field collected and synthetic FPW in order to determine the effect of organic compounds in FPW on sorbent performance and structure.

2. Materials and methods

2.1. Reagents

Lithium hydroxide (98%), manganese chloride tetrahydrate ($MnCl_2{\cdot}4H_2O$, >99%), hydrogen peroxide (H_2O_2, 30% in water), sulfuric acid (H_2SO_4, 98%), sodium hydroxide (NaOH, >99%), ammonium oxalate monohydrate ($(NH_4)_2C_2O_4{\cdot}H_2O$, >99%), potassium permanganate ($KMnO_4$, >99%), hydrochloric acid (HCl, 37% in water), sodium chloride (NaCl, >99%), lithium chloride (LiCl, >99%), microcrystalline cellulose, Triton X-100 (70% in water) and manganese dioxide (MnO_2, 98%) were purchased from Fisher Scientific, Canada. Lithium manganese dioxide ($LiMnO_2$, >99%) and lithium manganese (III, IV) oxide ($LiMn_2O_4$, >99%) were purchased from Sigma Aldrich, Canada. All solutions were prepared using deionized water with a resistivity of 18.2 MΩ cm at 25 °C.

2.2. Flowback and produced water

The FPW used in this study was collected in the field from a hydraulic fracturing well in the Duvernay Formation in Alberta, Canada in December 2016, 15 days after fracturing. A synthetic brine was prepared to mimic the inorganic composition of the FPW. Major properties of the fluids are listed in Table A.1.

To conduct experiments on filtered fluid samples, FPW was centrifuged at 4000 g for 5 min and the oil layer was removed. The fluid was then filtered through a 0.20 μm nylon syringe filter before ultra or nanofiltration. For ultrafiltration, the filtered FPW was passed through a Millipore Pellicon XL Cassette Biomax 10 kDa ultrafiltration membrane using a peristaltic pump, and for nanofiltration the FPW was passed through a 100–250 Da Synder Filtration NFS nanofiltration membrane using dead stop filtration at 5 bar. Major properties of filtered fluids are listed in Table A.2.

2.3. Sorbent preparation

Manganese based sorbents were prepared using a co-precipitation method similar to that used by Tian *et al.*, [21], without the addition of $Mg(NO_3)_2{\cdot}6H_2O$. 3.0 M LiOH was added in Li:Mn molar ratios of 2:1 and 3:1 to 0.375 M $MnCl_2$ solution at 20 °C to produce a slurry. 30% H_2O_2 was added dropwise to each solution to oxidize the Mn (II) and produce the manganese oxide precursor. Each solution was stirred for 2 h, transferred to a ceramic drying tray and dried in a forced air convection oven at 90 °C for 16 h. The resulting precursors were ground to a fine powder using a mortar and pestle and calcined in a furnace in air at 450 °C for 4 h. Each sorbent was then washed twice in 50 mL of deionized water, and the resulting products were designated lithium manganese oxides LMO-2 and LMO-3 for synthesis Li:Mn ratios of 2:1 and 3:1, respectively. Portions of each of these materials were stirred in 0.50 M H_2SO_4 at 20 °C for 1 h. The resulting protonated ionic sieves were washed twice in deionized water and designated as HMO-2 and HMO-3 for synthesis Li:Mn ratios of 2:1 and 3:1, respectively.

2.4. Sorption and desorption experiments

Optimization of lithium recovery conditions was performed as part of this study and can be referenced in Appendix A. FPW was centrifuged at 4000 g for 5 min and the oil layer was removed. The FPW was pipetted into a glass vial, and its pH was adjusted using 1.0 M NaOH. pH was measured using a Mettler Toledo FiveEasy Plus pH meter. The FPW was heated to 70 °C, and the protonated sorbent was added at a dosage of 2.0 g L^{-1} for a sorption time of 30 min with constant mixing. After sorption, the mixture was centrifuged at 4000 g for 5 min. The treated FPW was removed and the Li loaded sorbent was washed twice with 10 mL of deionized water. The Li loaded sorbent was then added to 0.5 M

H_2SO_4 at a dosage of 6.0 g L^{-1} and was stirred at 20 °C for 5 min. After desorption, the mixture was centrifuged at 4000 g for 5 min. The acid was removed, the re-protonated sorbent was washed twice with deionized water, and the sorbent was dried in open air at 20 °C.

FPW samples were taken after pH adjustment and after Li recovery and were analyzed for major elements using an Agilent 8800 Triple Quad Inductively Coupled Plasma – Mass Spectrometer (ICP-MS/MS). Elements measured in the FPW were Li, B, Na, Mg, K, Ca, Mn and Sr. Li uptake was determined using a mass balance between the pH adjusted and treated FPW. A sample of the desorption acid was analyzed using ICP-MS/MS for the same elements measured in the FPW samples to determine the lithium concentrate purity, and Mn concentrations were used to calculate sorbent loss in the acid.

2.5. Chemical analyses

2.5.1. Manganese average oxidation state determination

Manganese average oxidation state (Z_{Mn}) was determined using a method similar to that outlined by Freeman and Chapman [22]. 180 mg of sorbent was digested in 25 mL of 0.10 M $(NH_4)_2C_2O_4$ + 12.5 mL of 4.0 M H_2SO_4 at 80 °C until complete dissolution was reached. The digestions were then back-titrated using 0.010 M $KMnO_4$ to a faint pink endpoint in order to determine the moles of oxalate which reacted, and therefore the moles of electrons which were transferred during the digestion step.

Mass percentages of Mn and Li in each sorbent were determined by digesting 40 mg of sorbent in 20 mL of 6.0 M HCl + 1.0 mL of 30% H2O2 at 80 °C for 1 h. Samples were then analyzed for Mn and Li concentrations using ICP-MS/MS; subsequently, the total moles of Mn in the sorbent used in the oxalate digestion was determined. Z_{Mn} was then calculated using the total moles of Mn in conjunction with the total moles of transferred electrons between oxalate and Mn determined by the titration. The Li:Mn molar ratio determined using ICP-MS/MS, in combination with Z_{Mn}, was then used to calculate a chemical formula for each sorbent in the form of LixMnyO4 [23].

2.5.2. Li selectivity Titrations:

Selectivity titrations were performed using a method similar to that outlined by Ooi *et al.,* [24]. 50 mg portions of protonated sorbent were added to 5.0 mL of 0.10 M solutions of MOH + MCl (M = Li or Na) in varying ratios of hydroxide to chloride. Blank titrations of NaOH + NaCl in the absence of sorbent were also prepared. The mixtures were stirred on a shaker table at 375 rpm at 20 °C for 6 h, and the pH of the supernatant of each solution was measured after sorption. Samples of the Li solutions were taken before and after sorption and analyzed using ICP-MS/MS to determine maximum Li uptake.

2.6. Physical analyses

Fourier-transform infrared spectroscopy (FTIR), thermogravimetric analysis (TGA) and X-ray diffraction (XRD) were all performed on 10 mg samples of dry sorbent. FTIR was performed using a Bruker Alpha FTIR Spectrometer, and absorbance values were collected in the wavenumber range of 750 – 4000 cm^{-1}. TGA was performed using a TA Instruments TGA Q50 using nitrogen gas, increasing the temperature from 20 °C to 1000 °C at a rate of 10 °C min^{-1}. XRD patterns were obtained using a Rigaku Ultima IV with a cobalt tube radiation source at 38 kV and 38 mA. Scans were performed using a range of 5°– 90° and a step size of 0.0200°. XRD patterns were interpreted and converted to a copper source using JADE 9.6 software.

Mn K-edge X-ray absorption spectroscopy (XAS) measurements were performed at beamline B18 at the Diamond Light Source, U.K. Samples were prepared by diluting 5 mg of sorbent in 150 mg of microcrystalline cellulose and mixing using a mortar and pestle. The mixture was then pressed into a 13 mm diameter pellet using a hydraulic press. Incident X-ray wavelengths were selected using a fixed exit double-crystal monochromator (with Si(1 1 1) and Si(3 1 1) crystals) [25,26]. XAS spectra were collected in transmission mode using two gas-filled ionisation chambers [25,26]. Mn metal foil was placed in front of a third ionisation chamber in order to correct for instrument drift [25]. For each sample, scans were performed in triplicate and the data were averaged and normalised using the program ATHENA [27] to produce X-ray absorption near edge structure (XANES) and extended X-ray absorption fine structure (EXAFS) spectra. k^3 weighted EXAFS spectra were modelled using ARTEMIS software, which uses structural models produced from published crystal structures [27], to determine interatomic Mn-O and Mn-Mn distances within each sample. Z_{Mn} from XANES spectra were determined using linear combination modelling in ATHENA; $LiMnO_2$, $LiMn_2O_4$ and MnO_2 were used as reference materials for Z_{Mn} of 3.0, 3.5 and 4.0, respectively.

A Kratos Ultra DLD X-ray Photoelectron Spectrometer (XPS) was used to acquire the near surface (< 10 nm) elemental composition and manganese oxidation states. A monochromatic Al source was used at 150 W power to obtain survey scans and Mn 2p, Mn 3p, and Mn 3 s high resolution spectra from the near surface region. The pass energy for narrow scans was 20 eV. Charge neutralization was used during acquisition. 99.9% pure Au reference powder was used to calibrate the spectra for Au $4f_{7/2}$ to 84.0 eV. Three areas per samples were analyzed. Shirley background was used to process the spectra. Quantification utilized sensitivity factors that were provided by the manufacturer. A 70% Gaussian / 30% Lorentzian (GL (30)) line shape was used for the curve fittings. Constraints used in curve fitting of Mn 2p, Mn 3p, Mn 3 s spectra were established in a previous study [28]. Multiplet splitting of Mn 3 s high resolution spectra was used to determine the oxidation state of Mn, also described in a previous study [28]. Additionally, the oxidation state of Mn was confirmed by observing the shape and position of Mn 3p high resolution spectra.

For the transmission electron microscope electron energy loss spectroscopy (TEM-EELS) data, images were acquired using a Thermo Scientific Talos 200X microscope equipped with an extreme field emission gun (X-FEG) source. The microscope was operated at 200 kV in STEM mode, resulting in a point resolution of < 0.16 nm. EELS data were acquired using a Gatan Continuum S system equipped with a complementary metal oxide semiconductor (CMOS) detector. Data were acquired using a dispersion of 0.15 eV $channel^{-1}$ and a constant drift tube voltage was used for standards and test samples. Spectra processing and generation of maps were performed using GMS 3.4 software with plural scattering removed by deconvolution.

Transmission electron microscope (TEM) images were acquired using a Philips/FEI (Morgagni) TEM along with a Gatan digital camera. Sorbent samples were dispersed in a 0.10 mg mL^{-1} suspension and a drop of the suspension was placed onto a TEM grid for analysis. Nitrogen adsorption/desorption isotherms at 77 K were obtained using a Quantachrome Autosorb- iQ -MP/XR and specific surface area was calculated using the Brunauer-Emmett-Teller (BET) method. Prior to analysis, each 200 mg sorbent sample was outgassed at 200 °C for 6 h. Zeta potential was measured with a Malvern Zetasizer using the Smoluchowski equation for analysis. Samples measured were 0.10 mg mL^{-1} suspensions of sorbent in deionized water at varying pH values. pH was adjusted using HCl or NaOH.

2.7. Fluid property analysis

Fluid samples were diluted 50:1 (v/v) in deionized water prior to both non-purgeable organic carbon (NPOC) and total inorganic carbon (TIC) analyses. A Shimadzu TOC-L CPH Model Total Organic Carbon Analyzer with an ASI-L TOC autosampler was used for both analyses. For NPOC measurement, samples were acidified using 1 M HCl before being sparged in order to strip the sample of purgeable organic and inorganic carbon. The sample was subsequently injected into a combus-

tion tube containing platinum catalyst beads at 720 °C in order to evolve the remaining carbon in the sample to CO_2, which was then measured using a non-dispersive infrared (NDIR) detector. For TIC measurement, the sample was injected into a bubble chamber, and phosphoric acid (25%) was added to react with the inorganic carbon, forming CO_2 gas. The sample was bubbled with air, and the evolved CO_2 was measured using an NDIR detector.

3. Results and discussion

3.1. Characterization of initial sorbents

3.1.1. Structural analysis

Spinel lithium manganese oxides sorb lithium via two proposed reversible sorption mechanisms: a redox mechanism and an ion exchange mechanism, as can be seen in Equations 1 and 2, respectively [17,23].

$$4\,(Li)\left[Mn^{3+}Mn^{4+}\right]O_4 + 8H^+ \rightarrow 3()\left[Mn_2^{4+}\right]O_4 + 4Li^+ + 2Mn^{2+} + 4H_2O \quad (1a)$$

$$()\left[Mn_2^{4+}\right]O_4 + nLiOH \rightarrow (Li_{n\,1-n})\left[Mn_n^{3+}Mn_{2-n}^{4+}\right]O_4 + \frac{n}{2}H_2O + \frac{n}{2}O_2 \quad (1b)$$

$$Li_xMn_yO_4 + xH^+ \leftrightarrow H_xMn_yO_4 + xLi^+ \quad (2)$$

These materials are selective toward lithium (under alkaline conditions) and protons (under acidic conditions) due to the small ionic radii of lithium ions and of protons [29–31]. Manganese in these sorbents can exist in both trivalent and tetravalent states; materials with higher proportions of trivalent manganese have a higher proportion of redox sites, while sorbents with exclusively tetravalent manganese contain exclusively ion exchange sites [17,23,24,32–35]. At a redox site, lithium desorption in acid is associated with reductive dissolution of trivalent to divalent manganese (Eq. (1a)), resulting in a net loss of sorbent with each sorption/desorption cycle [17,23]. For this reason, the optimum, highest stability manganese based sorbent would contain exclusively tetravalent manganese [30].

Table 1 summarizes the results from the structural analysis of LMO/HMO-2 and LMO/HMO-3. LMO/HMO-3 was determined by XRD to be pure ion exchange $Li_{1.33}Mn_{1.67}O_4$, while LMO/HMO-2 contains a mix of $Li_{1.33}Mn_{1.67}O_4$ and low valence manganese (III) phases. FTIR and TGA reveal that both sorbents exhibit an ion exchange mechanism, however HMO-3 has more than triple the ion exchange site concentration than HMO-2 and is therefore expected to be the better lithium sorbent.

Z_{Mn} of sorbent LMO-2 and its protonated counterpart HMO-2 were determined to be 3.47 and 3.64, respectively, resulting in a chemical formula of $Li_{0.91}Mn_{2.04}O_4$ calculated for LMO-2. The prevalence of Mn (III) in this sorbent expressed by its low Z_{Mn} value indicates the presence of redox sites in this sorbent [23,24,32–35]. LMO-3 and HMO-3 had Z_{Mn} of 3.87 and 3.99, respectively, resulting in a chemical formula of $Li_{1.47}Mn_{1.69}O_4$ for LMO-3. HMO-3's oxidation state is consistent with a sorbent with almost exclusively ion-exchange sites [23,24,32–35]. Z_{Mn} in both sorbents increased significantly after the initial protonation step due to acid dissolution of low valence manganese in the bulk material [23,24]. Dissolution of low valence manganese phases would also lead to the tighter distribution of Mn-Mn distances determined by EXAFS between the LMO and HMO versions of each sorbent (Table 1).

FTIR spectroscopy (Fig. 1(a)) demonstrates that both HMO-2 and HMO-3 experienced proton insertion into their structures during acid treatment, indicating that both sorbents contain ion exchange sites.[36] The absorbance peak at 3330 cm^{-1} can be attributed to stretching vibrations of hydroxyl groups within the lattice, the peak at 1600 cm^{-1} is due to bending vibrations of hydroxyl groups, and the peak at 900 cm^{-1} is due to lattice vibrations of protons [37].

TGA data for both protonated sorbents shows mass loss between 150 and 300 °C, which further indicates the presence of ion exchange sites in the sorbents [23,24,30,32,34,37]. This mass loss, centered around 220 °C, has been attributed to structural water loss from condensation of lattice hydroxyl groups, which were formed during ion exchange with lithium, within the spinel structure of the sorbent [23,34,37]. In this way, the total proton content of the protonated sorbent, and therefore the concentration of ion exchange sites, can be determined from the mass loss between 150 and 300 °C.[23] HMO-2 experienced a 1.97% mass loss in this temperature range as compared to a 6.18% loss by HMO-3, indicating that HMO-3 contains >3 times more ion exchange sites than HMO-2. The redox site concentration can then be calculated

Table 1
Summary table of physical and chemical characteristics of initial calcined and protonated sorbents.

Sorbent	Z_{Mn}	Chemical Formula (Feng *et al.*, [23] method)	Ion Exchange Site Fraction	Redox Site Fraction	BET Surface Area ($m^2\ g^{-1}$)	Pore Volume ($cm^3\ g^{-1}$)	EXAFS Mn-Mn distances	
							R (Å)	σ (Å)
LMO-2	3.47	$Li_{0.91}Mn_{2.04}O_4$	–	–	15	0.22	2.90	0.088
HMO-2	3.64	$Li_{0.17}H_{0.42}Mn_{2.04}O_4$	79%	21%	33	0.26	2.87	0.083
LMO-3	3.87	$Li_{1.47}Mn_{1.69}O_4$	–	–	25	0.07	2.89	0.087
HMO-3	3.99	$Li_{0.12}H_{1.21}Mn_{1.67}O_4$	98%	2%	74	0.25	2.87	0.079

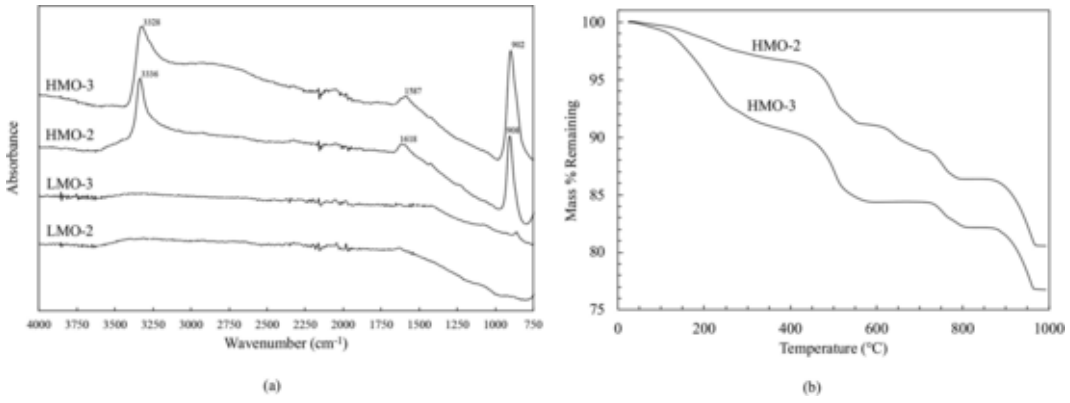

Fig. 1. FTIR (a) and TGA (b) comparison plots of initial calcined (LMO) and protonated (HMO) sorbents.

from the ratio of Li to Mn in the desorption acid [23]; site evaluation results are listed in Table 1. After determining proton content, chemical formulas were assigned to the protonated sorbents using the method outlined by Feng *et al.*, [23]

Site evaluation results for HMO-3 reveal a 98% proportion of ion exchange sites, which is consistent with its Z_{Mn} of 3.99 [23,24,32–35]. Site evaluation results for HMO-2 show an ion exchange site percentage of 79%, signifying that it is primarily an ion exchange sorbent as well. This is atypical given the high proportion of Mn (III) in its structure, which is associated with the presence of redox sites [23,24,32–35]. The prevalence of Mn (III) in HMO-2 was therefore hypothesized to be dominantly in the form of a separate Mn (III) phase in the bulk material which did not participate in the lithiation/delithiation reactions. This hypothesis is supported by the Z_{Mn} increase to only 3.64 after acid treatment; in a pure redox type sorbent such as $LiMn_2O_4$, Z_{Mn} increases to 4.0 after delithiation [23]. These additional Mn (III) phases would impact the resulting chemical formulas calculated using the Feng *el al.*, [23] method for LMO-2 and HMO-2; this hypothesis also helps to explain why the formula for LMO-2 falls outside of the spinel lithium manganese oxide formula range of $(Li)[Li_xMn_{2-x}]O_4$, $0 \leq x \leq 0.33$ [34].

XRD patterns (Fig. 2) for LMO-3 and HMO-3 confirm its spinel structure, and display a pattern consistent with that of the ion-exchange sorbent $Li_{1.33}Mn_{1.67}O_4$. The similarity between the XRD patterns for LMO-3 and HMO-3 indicates that delithiation occurred topotactically during acid treatment, preserving the original spinel structure [34]. Three different phases were identified in the XRD patterns of LMO-2 and HMO-2: $Li_{1.33}Mn_{1.67}O_4$, Mn_2O_3 and $Mn_8O_{10}Cl_3$ ($Mn_8O_{10}Cl_3$ can be produced during calcination of MnO_2 + $MnCl_2$ above 300 °C [38]). The presence of one or both of these low valence manganese impurities in LMO/HMO-2 is supported by both the XPS and EXAFS analyses. EXAFS revealed a larger distribution of Mn-Mn interatomic distances in HMO-2 species compared to those in HMO-3 species (Table 1, Table A.3). This could be explained by HMO-2 species being comprised of a mix of separate manganese phases. Furthermore, the LMO/HMO-2 species could not be adequately fit using EXAFS without the addition of 30% Mn_2O_3 or $Mn_8O_{10}Cl_3$ to the $Li_{1.33}Mn_{1.67}O_4$ model (Fig. 3). XPS detected Mn (III) on the surface of LMO-2 (Table A.5), and Cl was detected on the surface of LMO-2 during the XPS elemental mapping, further supporting the XRD evidence of Mn_2O_3 and $Mn_8O_{10}Cl_3$ phases in LMO-2. This supports our earlier hypothesis that delithiation could have occurred primarily at the ion exchange sites in the sorbent, while the Mn (III) phases were not significantly affected during acid treatment. A Z_{Mn} of 3.64 in the delithiated sorbent suggests that HMO-2 may consist of >30% non lithium-exchanging Mn (III) phases; it can therefore be concluded that for the co-precipitation method employed in this research, a large excess of Li (Li:Mn of 3) is required during synthesis in order to avoid production of these phases.

EXAFS data for calcined and protonated versions of each sorbent indicate a contraction of the crystal structure of the sorbents after protonation [39–41]. This is evidenced by the decreased distance between Mn-Mn atoms between the LMO and HMO versions of each sorbent, as displayed in Table 1. These Mn-Mn distances increase again after relithiation, and subsequently decrease after lithium desorption (Table A.3), suggesting that the crystal structure of the sorbent expands during lithium insertion and contracts during lithium desorption in every cycle. Similar results have been reported in previous studies [39–41] which use EXAFS analysis on manganese based ion exchange materials.

TEM images of both calcined and protonated sorbents are displayed in Fig. 4. LMO-2 and HMO-2 appear to consist of a combination of long (>100 nm length) needle shaped particles as well as some small (<100 nm diameter) cubic shaped particles. LMO-3 and HMO-3 are comprised of almost exclusively small, cubic shaped particles. The larger particles comprising HMO-2 result in a smaller BET surface area of 33 $m^2\ g^{-1}$, compared to 74 $m^2\ g^{-1}$ for HMO-3. The surface areas of both sorbents more than doubles after the initial protonation step (between their LMO and HMO versions); this result was also found by Wang *et al.*, [34], and can be attributed to dissolution of Mn (II) and opening of pores in the structure after first exposure to acid [33,42]. This is supported by the measured increase in pore volume in both sorbents after protonation (Table 1).

3.1.2. Behavior in solution

Both HMO-2 and HMO-3 have a point of zero charge (PZC) in solution close to pH 2 (Figure A.10(b)). This indicates that both sorbents should exhibit good dispersion at typical Li sorption conditions of pH 6 and higher [21]. HMO-2 has a significantly more negative zeta potential than HMO-3 when pH ≥ 4. HMO-3 is shown by TGA data to contain more hydroxyl groups than HMO-2; a higher concentration of hydroxyl

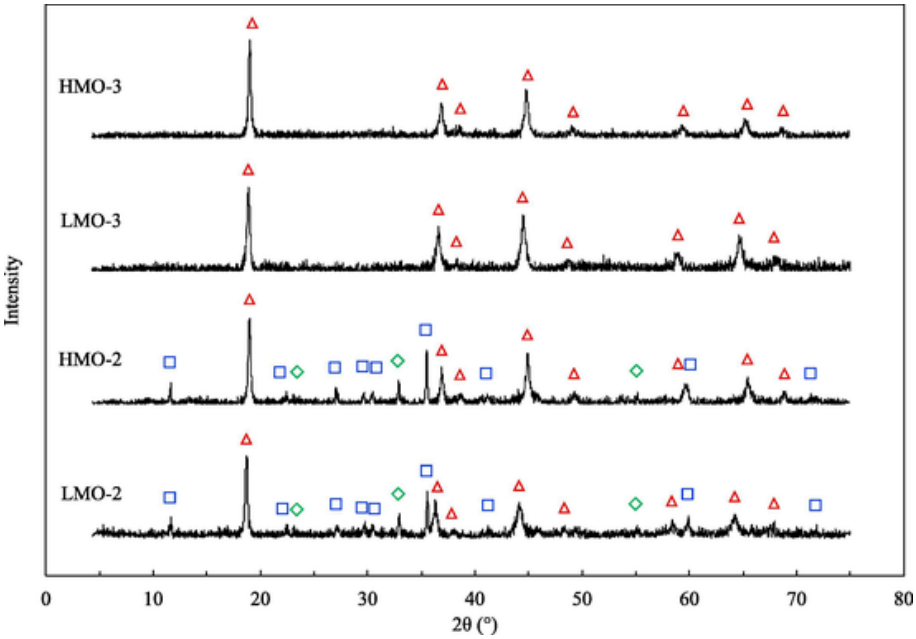

Fig. 2. XRD comparison plot of initial calcined and protonated sorbents. ◇, □ and △ represent peaks which can be attribued to Mn_2O_3, $Mn_8O_{10}Cl_3$ and $Li_{1.33}Mn_{1.67}O_4$ phases, respectively.

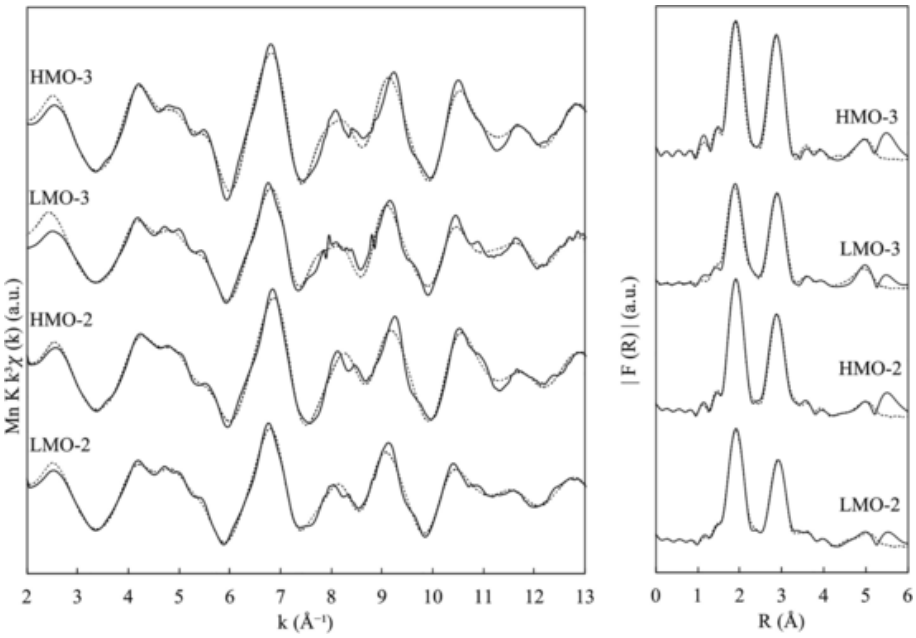

Fig. 3. Mn K-edge EXAFS and Fourier transforms for initial calcined and protonated sorbents. Dashed lines represent fits for each material. LMO/HMO-3 species were fit using a pure $Li_{1.33}Mn_{1.67}O_4$ model, whereas LMO/HMO-2 species were fit using a 70% $Li_{1.33}Mn_{1.67}O_4$, 30% Mn_2O_3 model; dashed lines represent fits for each material.

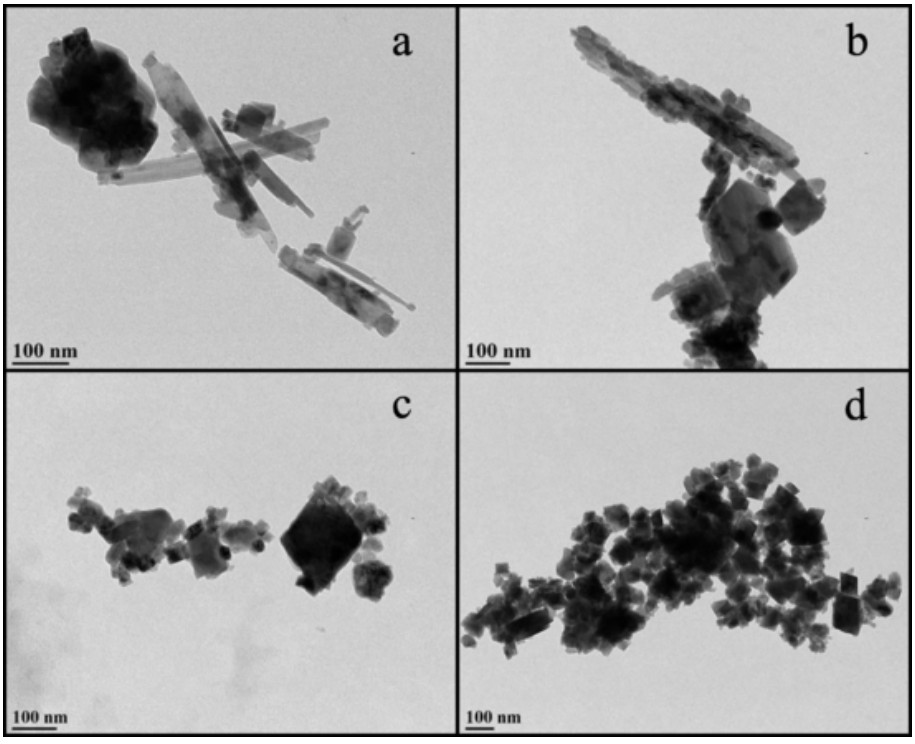

Fig. 4. TEM images of LMO-2 (a), HMO-2 (b), LMO-3 (c) and HMO-3 (d).

groups would typically lead to a more negative zeta potential [43]. The intramolecular hydroxyl groups associated with Li-specific ion exchange sites in HMO species, however, are not surface functional groups, and will therefore only interact with the solution if Li ions are present [29–31], as exhibited in Figure A.10(a). Therefore, the lattice hydroxyl groups measured by TGA would not contribute to the measured zeta potential. One potential explanation for the discrepancy in zeta potential is that HMO-2 may have more negative surface functional groups present on its Mn (III) phases. $Mn_8O_{10}Cl_3$ contains oxychloride surface functional groups capable of inner sphere complexation and has been used for nonspecific cation surface sorption in previous literature, suggesting it should exhibit a more negative zeta potential in solution [44,45].

Data from Li selectivity titrations can be referenced in Figure A.10 (a). For both protonated sorbents, the pH vs. meq OH^- curve under immersion in a NaOH/NaCl solution essentially follows that of the blank titration containing no sorbent, indicating little or no ion exchange between Na ions in solution and protons in the sorbents [23,24,32]. When immersed in a LiOH/LiCl solution, both sorbents exhibited ion exchange between Li and protons, releasing protons into solution and

buffering its pH [23,24,32]. This experiment verifies that both HMO-2 and HMO-3 are Li selective ion exchange sorbents. HMO-3 was able to buffer the solution at higher concentrations of OH^- than HMO-2 due to its higher concentration of ion exchange sites [23,24,32]. The maximum Li uptake by HMO-2 and HMO-3 in these experiments were 18 mg g^{-1} and 27 mg g^{-1}, respectively; these values represent the maximum projected Li sorption capacities of these materials from FPW. Interestingly, there was an observed production of permanganate from both HMO-2 and HMO-3 in Li titrations in which the final pH was > 10, which did not occur in the Na titrations (Figure A.14). A similar result was found by Feng *et al.*, [32] using a similar experiment. Saenko *et al.*, [46] attributed this phenomenon to the redox disproportionation reaction $4Mn^{4+} \rightarrow 3Mn^{3+} + Mn^{7+}$ during lithium sorption, resulting in the release of MnO_4^-. See (Fig. 5.).

3.2. Sorbent performance in FPW

3.2.1. Optimization of sorption/desorption conditions

Optimization of experimental conditions has been completed for the FPW tested in this research and can be referenced in Appendix A. These experimental conditions include sorption pH, sorption temperature and time, sorbent dosage ratio, desorption time and acid concentration; conditions were originally optimized using HMO-2, and the same conditions were later applied when using HMO-3 for consistency. See (Fig. 6.).

Sorption pH has a significant impact both on lithium uptake and on the final lithium concentrate purity due to proton release at ion exchange sites during lithium sorption, causing a fluid pH drop [21]. With an initial sorption pH of 8 and higher, HMO-2 was able to reach its maximum lithium uptake prior to the pH of solution dropping to a level below that required for lithium-proton ion exchange (Figure A.1). Conversely, an initial pH of 8 and lower resulted in fewer impurities in the final lithium concentrate; at sorption conditions of pH 9 and higher, un-

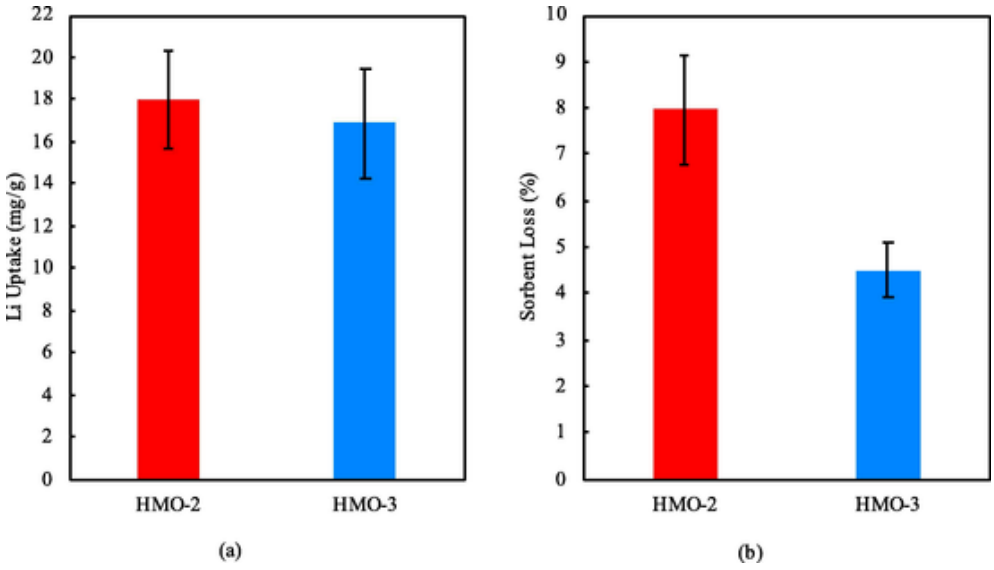

Fig. 5. Li uptake (a) and sorbent loss in acid (b) of HMO-2 and HMO-3 during Li recovery from FPW. Error bars represent 1 standard deviation.

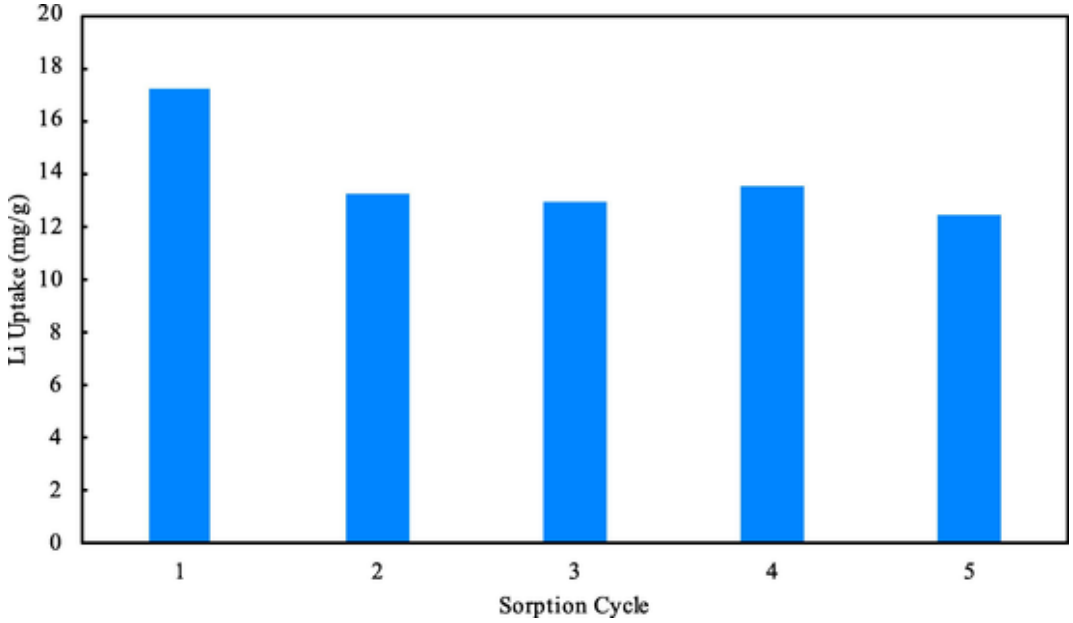

Fig. 6. Li uptake when recycling HMO-3 in FPW with a 1% Triton X-100 solution wash following each desorption cycle.

desired cations precipitated from solution and were not separated during centrifugation, leading to high Na, Mg and Ca concentrations in the final concentrate (Figure A.2). Sorption kinetics and final uptake were highly dependent on sorption temperature (Figure A.3); at a sorption temperature of 70 °C (the FPW wellhead temperature), a maximum lithium uptake of 17 mg g^{-1} was reached in 30 min, versus a maximum uptake of 12.5 mg g^{-1} after 4 h at 20 °C. Sorbent dosage had a significant impact on lithium extraction efficiency and on lithium uptake due to differences in the decrease of FPW pH during sorption (Figure A.5). It was found that a dosage of 2.0 g L^{-1} resulted in the best balance between extraction efficiency and lithium uptake for the previously determined sorption conditions (Figure A.4). Desorption performance was less sensitive to the tested conditions as compared to sorption; desorption kinetics were fast, reaching maximum stripping efficiency after 5 min (Figure A.6), and acid concentration had little effect on stripping efficiency (Figure A.7), with the exception of desorption in 10 mM H_2SO_4. In this experiment, there were fewer total moles of protons in the acid than there were moles of lithium in the sorbent, causing the acid to be completely neutralized prior to complete lithium desorption. These experiments utilized a lithium concentration factor (volume ratio of FPW to desorption acid) of 3.0; producing a more concentrated lithium product would require a more concentrated acid in order to avoid neutralization. Sorbent dissolution in acid was not affected by the tested desorption conditions. See (Fig. 7.).

For these reasons, the optimum lithium recovery conditions were determined to be sorption at pH 8 and 70 °C for 30 min with a sorbent dosage of 2.0 g L^{-1}, followed by desorption in 0.5 M H_2SO_4 for 5 min. At these conditions, HMO-2 was able to extract >80% of the lithium from the FPW, with an average uptake of 18 mg g^{-1}. Using a concentration factor of 3.0, the lithium stripping efficiency was 98%, leading to a relatively pure product containing 15 mmol L^{-1} of lithium (Figure A.8). Further processing of this concentrate using techniques such as solvent extraction to remove boron would likely be required to improve the purity of the concentrate before further processing. These conditions were used for all lithium sorption and desorption experiments in the following sections.

3.2.2. Sorption and desorption experiments under optimized conditions

Average first cycle lithium uptake from FPW was comparable between HMO-2 and HMO-3 at approximately 18 mg g^{-1} and 17 mg g^{-1}, respectively. This is consistent with the maximum lithium uptake determined in the selectivity experiments for HMO-2 (18 mg g^{-1}); however, HMO-3 displayed a significantly lower Li uptake from FPW as compared to its maximum uptake of 27 mg g^{-1} determined from the selectivity experiments. This is due to the pH drop (Figure A.5) of the FPW during lithium sorption due to protons being released from ion exchange sites [21]. At ion exchange sites, lithium sorption is significantly impeded when the solution pH drops below 6 [21], and effectively ceases below pH 4 [23], meaning that the maximum uptake capacity cannot be reached if the pH drops below this threshold during sorption. Experimental conditions were initially optimized for sorption using HMO-2; a higher FPW starting pH would be required for HMO-3 to reach its maximum uptake.

First cycle sorbent loss in acid fluctuated considerably for both sorbents, but was typically between 4% – 10%. Literature values for sorbent loss during acid desorption from redox-type $LiMn_2O_4$ can be as high as 27% [47]. Pure ion-exchange type $Li_{1.33}Mn_{1.67}O_4$ exhibits far lower sorbent loss due to the lack of a reductive dissolution mechanism [30,48]. Manganese dissolution from a pure ion exchange sorbent occurs primarily due to the presence of a few Mn (III) atoms present in the bulk material; the trivalent manganese transfers electrons to Mn (IV) atoms on the particle surface during acid treatment, resulting in the formation and release of Mn (II) [49]. Due to this mechanism, pure ion exchange $Li_{1.33}Mn_{1.67}O_4$ and $Li_{1.6}Mn_{1.6}O_4$ sorbents typically experience between 1% – 2% sorbent loss per cycle [30,48]. Experimental sorbent loss values after sorption from FPW were therefore within a potential range for a sorbent containing redox-type sorption sites such as HMO-2, but were significantly higher than literature values for a pure ion exchange sorbent such as HMO-3. We therefore speculated that exposure to FPW during lithium sorption leads to an increased sorbent loss in the subsequent desorption step.

3.2.3. Sorbent recycling

Recycling of spinel lithium manganese oxide sorbents in brine has previously provided positive results in literature. Tian *et al.*, [21] and Ooi *et al.*, [31] both found the drop in lithium uptake to be negligible over the course of 5 cycles. Recycling of both HMO-2 and HMO-3 in FPW, however, proved to be challenging in this study. Initial recycle testing was performed on HMO-2, and the methodology which resulted in the most positive outcome was later confirmed to perform similarly on HMO-3.

With no treatment to the FPW, second cycle lithium uptake by HMO-2 dropped markedly to 2 mg g^{-1}, compared to the first cycle uptake of 17 mg g^{-1} (Figure A.9). On the second sorption cycle, the sor-

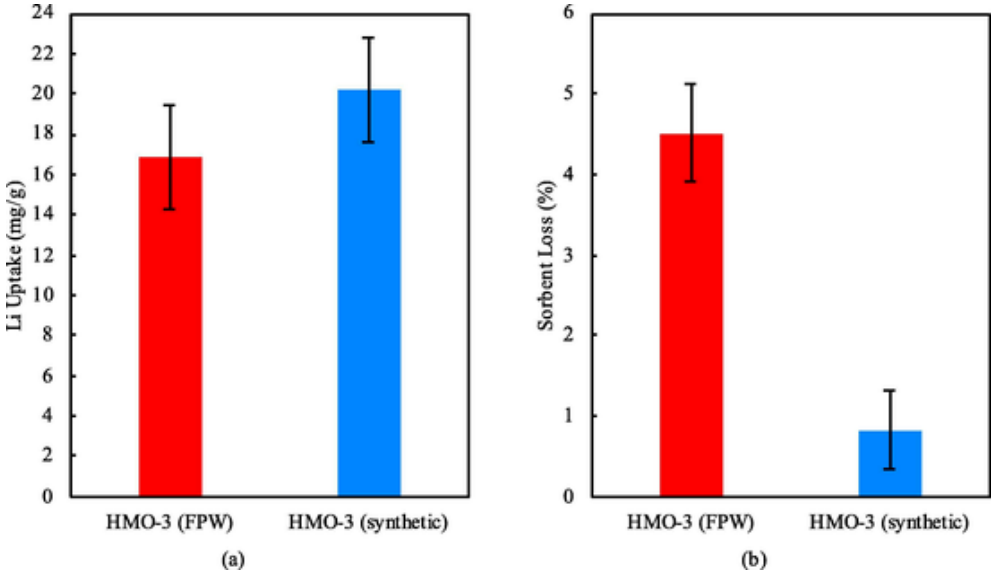

Fig. 7. Li uptake (a) and sorbent loss in acid (b) of HMO-3 during Li recovery from FPW and synthetic brine. Error bars represent 1 standard deviation.

bent was observed to aggregate and float on top of the FPW instead of dispersing as usual. We hypothesized that a coating of non-aqueous organic liquids present in the FPW was formed on the sorbent surface during the first sorption that was carried through the washing and drying process, as reported previously for titanium-based sorbents [50,51]. This hypothesized coating could cause the sorbent to become hydrophobic, reducing its reactive surface area and therefore reducing its sorption capacity. In an attempt to avoid the buildup of any organic coating on the sorbent surface, various organic removal treatments were studied (Figure A.9); it was determined that the most effective solution was a surfactant (1% Triton X-100) wash after each sorption cycle prior to drying. Using this method, lithium uptake plateaued at 13 mg g^{-1} between cycles 2–5 after a first cycle uptake of 17 mg g^{-1}, supporting the presence of an organic coating and indicating that the surfactant was successful in its removal.

3.3. Effect of organic fracturing additives on sorbent performance and structure

3.3.1. Sorbent performance in synthetic brine

In order to study the impact of FPW on sorbent loss, a synthetic brine was prepared to replicate the inorganic characteristics of the FPW in the absence of any of the organic content. Sorption and desorption experiments were performed on HMO-3 at the previously determined optimized conditions. HMO-3 was used exclusively in these initial experiments due to the large discrepancy between experimental sorbent loss and literature values for similar sorbents [30,48]. Li uptake from the synthetic brine by HMO-3 was, on average, slightly higher that from the FPW at 21 mg g^{-1}. This is likely due to the synthetic brine having a higher buffering capacity, which limits the pH drop during sorption; the final pH values of the treated fluids were 5.5 and 5.9 for FPW and synthetic brine, respectively. More significantly, first cycle sorbent loss from HMO-3 was considerably lower with synthetic brine than with FPW at 0.8% on average, which is more typical for a pure ion exchange sorbent [30,48]. We therefore hypothesized that organics present in the FPW were reducing Mn (IV) in the sorbent during lithium sorption, leading to a consequent increase of Mn dissolution in acid.

3.3.2. Manganese reduction in FPW

In order to test our hypothesis of Mn reduction by organic compounds, sorption experiments with HMO-2 and HMO-3 were performed in both field collected FPW and synthetic brine, and samples of the sorbents were analyzed after lithium loading and after acid desorption. Z_{Mn} measurements for each experiment are presented in Fig. 8. After both Li loading from synthetic brine and subsequent acid desorption, Z_{Mn} of HMO-3 remains at 4.0, resulting in a low sorbent loss of 0.7% for the cycle. Z_{Mn} of HMO-2 drops from 3.64 to 3.59 after Li insertion in synthetic brine due to the presence of redox sites in the sorbent [23,24,32–35]. Acid desorption results in a 3.1% sorbent dissolution and a slight increase of Z_{Mn} to 3.61 due to disassociation of the Mn (III) which was produced during Li sorption at redox sites [23,24,32–35].

Both HMO-2 and HMO-3 display a significant drop in Z_{Mn} (0.24 units of Z_{Mn} each) after sorption in the field collected FPW, substantiating our Mn reduction hypothesis. During subsequent Li desorption in acid, almost all of the Mn which was reduced by the FPW dissolves into solution, resulting in a 9.5% and 10.1% loss of HMO-3 and HMO-2, respectively, and an increase in Z_{Mn} to approximate pre-exposure values for both. This measured Z_{Mn} drop after sorption from FPW is corroborated by XANES data for both sorbents (Table A.4).

FPW has a highly complex organic profile because it is comprised of components from natural formation water and additives in the fracturing fluid along with their degradation products [9,20]. A previous study on FPW from the Duvernay Formation in Alberta determined that the most common dissolved organic species present were polyethylene glycols (PEGs), octylphenol ethoxylates (OPEs) and alkyl dimethyl benzyl ammonium chlorides (ADBACs) [20]. There is an abundance of evidence [52–59] of various easily oxidizable organics reducing manganese oxides in nature. Humic, fulvic, gallic, ascorbic and tannic acids, as well as a wide variety of small aromatic compounds which could be present in FPW, are all able to reduce MnO_x compounds to soluble Mn (II) [52,57]. When this occurs, Mn (IV) or Mn (III) is reduced to Mn (II) and is released into solution.

This does not appear to be the case during lithium sorption, however, as no measurable Mn was observed in the treated FPW after sorption, even in cases where the FPW pH dropped as low as 4.0. The Mn which is reduced during sorption necessarily exists as part of the bulk sorbent, leading to the measured drop in Z_{Mn} after sorption from FPW. This is further evidenced by the 2nd shell Mn-Mn distances measured by EXAFS (Table A.3); in both HMO-2 and HMO-3, the average 2nd shell Mn-Mn distances increase more significantly after lithium sorption from FPW as compared to from synthetic brine. Furthermore, the "lithium loaded from FPW" versions of each sorbent have the widest distribution of Mn-Mn distances compared to any other version of each sorbent. These two pieces of evidence indicate a change in the sorbent's

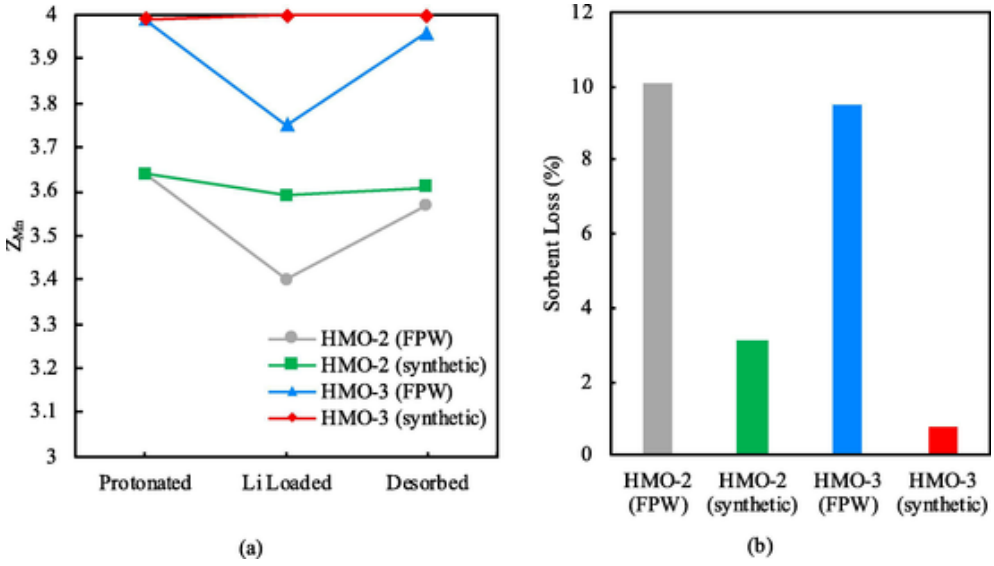

Fig. 8. Changes in Z_{Mn} throughout sorption/desorption cycle (a) and resulting sorbent loss in acid (b) of HMO-2 and HMO-3 during Li recovery from both FPW and synthetic brine.

structure during FPW exposure, likely due to the presence of reduced manganese. Both of these measurements in both sorbents are comparable to their synthetic brine experiment counterparts post desorption, indicating dissolution of these reduced manganese atoms in acid. In an attempt to visualize this manganese reduction by the FPW, and to determine whether the reduction occurs in the bulk or near the surface of the particles, TEM-EELS was performed on samples of HMO-3 after lithium loading from both FPW and from the synthetic brine (Fig. 9).

EELS line scans were performed across individual nanoparticles in order to visualize the spatial distribution of manganese valence. EELS is not a surface valence measurement technique; electrons which are measured have been transmitted through the entire depth of the three dimensional nanoparticle, and the data is then mapped onto a two dimensional image. Electrons which are transmitted through the sample near the edge of the particle in the two dimensional image can therefore be used to represent the outer surface of the nanoparticle; electrons which pass through the bulk of the particle, however, will carry a signal that represents the particle's bulk valence state as compared to its thin surface layer.

EELS data show that lithium loaded HMO-3 nanoparticles, both from synthetic brine and from FPW, have a thin (approximately 2 nm) layer of Mn (III) on the particle surface, and are primarily Mn (IV) in the bulk material (Fig. 9). The major observed difference between the two samples was that the majority of the nanoparticles analyzed from the synthetic brine had Mn valence distributions similar to particles (a) and (b) in Fig. 9, with a large majority of Mn (IV) in the particle interiors, which further supports the measured Z_{Mn} of 4.0 for these particles. Measured nanoparticles exposed to FPW, however, were all similar to particle (c), with a significant proportion of Mn (III) measured in the particle bulk. These results indicate that organic molecules are reducing Mn (IV) in the bulk of the nanoparticles to Mn (III) during lithium sorption in FPW, causing the measured drop in bulk Z_{Mn} of the particles after lithium sorption, and consequent Mn dissolution during acid desorption.

The cause of the thin layer of Mn (III) on the surface of the nanoparticles is not known; however, it is possible that it is formed during the initial protonation step during preparation of HMO-3 as discussed below. XPS results (Table A.5) express differences in the average Mn surface valence in the surface 5–10 nm of the nanoparticles using Mn 3 s multiplet splitting [28]. Somewhat counterintuitively, LMO-3 (Z_{Mn} 3.87) has a smaller Mn 3 s multiplet split than HMO-3 (Z_{Mn} 3.99), which would signify a higher proportion of Mn (IV) on the surface of LMO-3 as compared to HMO-3 [28]. This suggests that although the majority of the low valence Mn in LMO-3 is dissolved during protonation in acid, as there was more Mn (III) in the first 5–10 nm of the surface of HMO-3 particles compared to in LMO-3. One explanation for this would be that the 2 nm surface layer of Mn (III) seen in the particles in Fig. 9 formed during initial protonation in acid. Higher surface Mn 3 s multiplet splits compared to LMO-3 indicate that this layer is present in all protonated, Li loaded and desorbed versions of the sorbent (Table A.5). It is unclear whether this thin Mn (III) surface layer is caused by reduction of Mn (IV) on the particle surface by the acid solution, or if it is formed as Mn (III) in the bulk donates electrons to the particle surface during protonation as proposed by Gao *et al.*, [49]

In an attempt to remove redox-active organic molecules, FPW samples were filtered through both a 10 kDa ultrafiltration membrane to remove large organics, and through a 100–250 Da nanofiltration membrane to remove small organics. Ultrafiltration did not significantly impact the inorganic profile of the FPW; nanofiltration resulted in a 13% decrease in total divalent cation concentrations (Table A.2). After ultrafiltration, the NPOC of the FPW dropped from 180 ppm to 116 ppm, and sorbent loss in acid was not significantly affected. After nanofiltration, the NPOC of the FPW dropped further to 85 ppm, and the sorbent loss in acid after sorption from this fluid dropped to 3.0%. This represents the lowest experimental value recorded for sorbent loss by HMO-3 from the field collected FPW; however, it is still higher than the sorbent loss measured after sorption in synthetic brine. This would suggest that the manganese is being reduced by small organic molecules (< 250 Da) and that complete removal of these organics would lead to sorbent loss values approaching those from the synthetic brine experiments.

4. Conclusions

In this work, two spinel lithium manganese oxide sorbents were prepared under different conditions using a co-precipitation method. The resulting ionic sieves were characterized for their crystal structure and behavior in solution, and used to recover lithium from FPW originating from the Duvernay Formation in Alberta, Canada. We found that in order to achieve a pure ion exchange sorbent without the presence of low valence manganese impurities, a large excess of lithium was required during the synthesis process. The sorbent prepared with a lithium to manganese ratio of 3 contained almost entirely ion exchange lithium sorption sites, and exhibited a higher lithium sorption capacity and a higher chemical stability during acid desorption than that prepared with a lithium to manganese synthesis ratio of 2. For both materials, sorbent loss in acid was significantly higher after lithium extraction from field collected FPW compared to that after sorption from a synthetic brine. Manganese valence measurements of sorbent samples before and after lithium sorption and desorption from FPW and the synthetic brine revealed that, compared to the synthetic brine, exposure to FPW reduced the average valence of the manganese in the sorbent, and subsequent exposure to acid led to a high degree of sorbent dissolution. Further analysis by EXAFS and TEM-EELS revealed that FPW exposure causes significant changes in the bulk chemical structure of the sorbent, including increased 2nd shell Mn-Mn distances, as well as an increased abundance of trivalent manganese in the sorbent bulk. We hypothesized that dissolved organic molecules in the FPW were responsible for the measured bulk manganese reduction in the sorbent, and its resultingly lower chemical stability in acid. The high sorbent loss resulting from lithium recovery from FPW would be a significant barrier to commercialization of this technology, as recycling of the sorbent would be essential to the economic viability of this process if applied in the future. Partial removal of dissolved organic molecules using nanofiltration presented positive results, significantly reducing the degree of sorbent loss. It is expected that complete removal of organics from the FPW would yield sorbent loss results similar to those found during lithium recovery from synthetic brine; this would additionally improve recyclability by removing the need for a post-desorption surfactant wash. For these reasons, in order for this technology to be applied for lithium recovery from FPW commercially, organic removal pretreatment technologies such as nanofiltration and oxidation, among others, should be further studied. In addition to organic removal technologies, redox active lithium desorption agents, such as persulfates, should be tested with this technology in order to study the impact that they may have on preventing reductive dissolution.

Uncited references

[36,60,61].

Declaration of Competing Interest

The authors declare that they have no known competing financial interests or personal relationships that could have appeared to influence the work reported in this paper.

Acknowledgements

We would like to acknowledge the funding sources which helped to finance this project, including the Natural Sciences and Engineering Re-

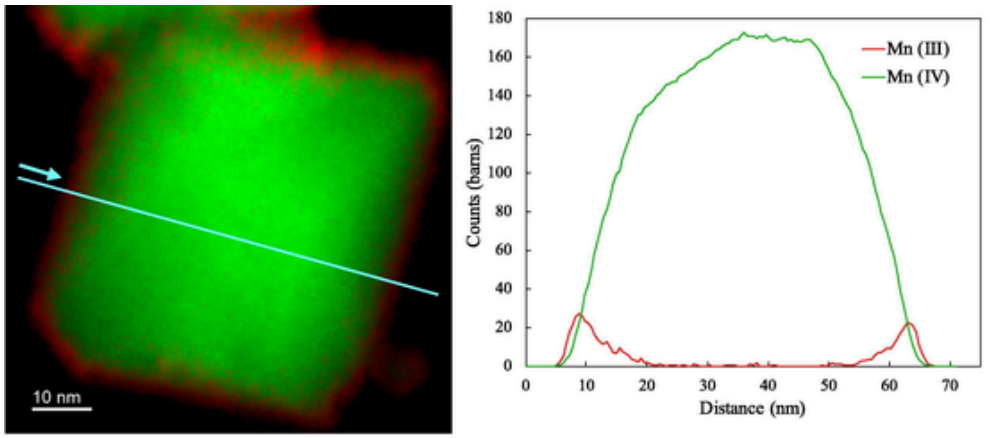
10 nm
Mn (III)
Mn (IV)
Counts (barns)
Distance (nm)
0
20
40
60
80
100
120
140
160
180
0
10
20
30
40
50
60
70

(a)

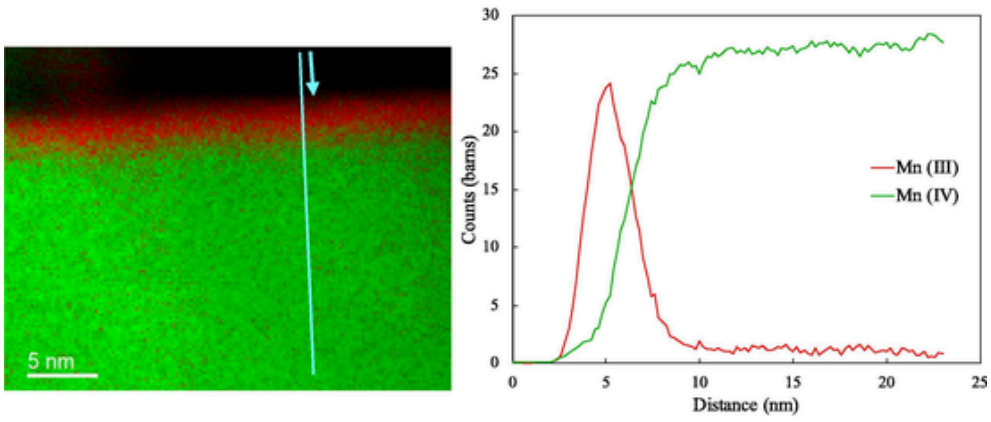
5 nm
Mn (III)
Mn (IV)
Counts (barns)
Distance (nm)
0
5
10
15
20
25
30
0
5
10
15
20
25

(b)

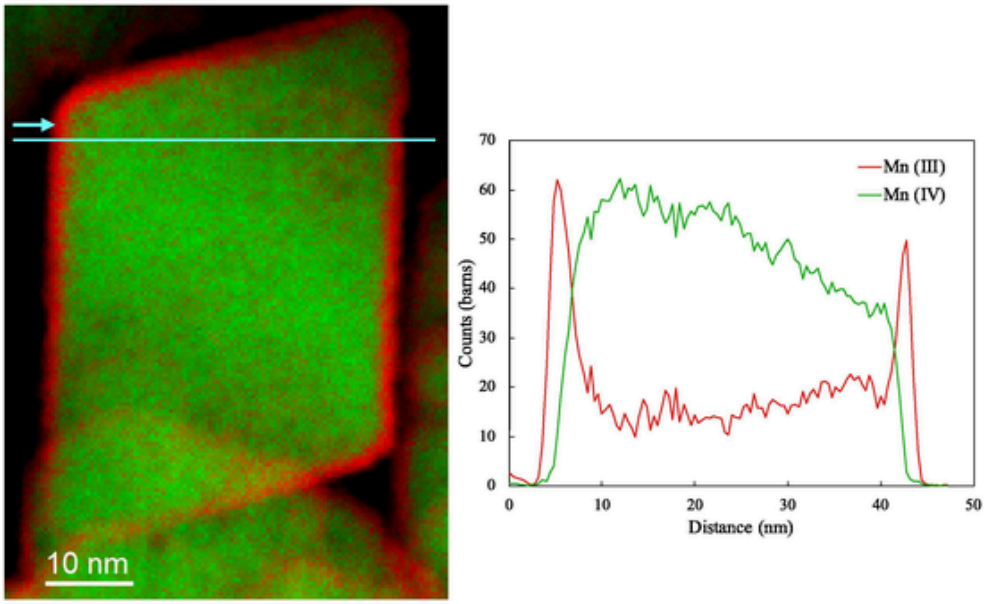
10 nm
Mn (III)
Mn (IV)
Counts (barns)
Distance (nm)
0
10
20
30
40
50
60
70
0
10
20
30
40
50

(c)

Fig. 9. TEM-EELS maps (left) displaying spatial distribution of relative abundances of Mn (III) (red) and Mn (IV) (green) in individual nanoparticles. The blue line running through each image represents the x-axis of its corresponding graph (right) showing relative abundance of Mn (III) and (IV) across a line scan running from zero in the direction of the arrow. Particles analyzed were Li loaded HMO-3 syn ((a) and (b)), and Li loaded HMO-3 FPW (c). (For interpretation of the references to colour in this figure legend, the reader is referred to the web version of this article.)

search Council of Canada (NSERC) for the award of a Canada Graduate Scholarship – Master's (CGS-M), Discovery Grant to DSA (RGPIN-04134), and a Collaborative Research and Development (CRD) grant to DSA (CRDPJ-519916).

Additionally, we would like to thank every person who helped perform the analyses required to complete this project, including Jonathan Banks and the people at the Advanced Water Research Lab at the University of Alberta. Finally, we thank the Diamond Light Source for the award of beam time as part of the Energy Materials Block Allocation Group SP14239.

Appendix A. Supplementary data

Supplementary Information for this article can be referenced in Appendix A. Supplementary data to this article can be found online at https://doi.org/10.1016/j.cej.2021.130713.

References

[1] F. Meng, J. McNeice, S.S. Zadeh, A. Ghahreman, Review of lithium production and recovery from minerals, brines, and lithium-ion batteries, Miner. Process. Extr. Metall. Rev. 42 (2) (2021) 123–141, https://doi.org/10.1080/08827508.2019.1668387.

[2] B. Swain, Separation and purification of lithium by solvent extraction and supported liquid membrane, analysis of their mechanism: a review, J. Chem. Technol. Biotechnol. (2016). https://onlinelibrary.wiley.com/doi/abs/10.1002/jctb.4976?casa_token=GoR3JIZ7iWwAAAAA:oN28ISlZvzodD0OhBk8j32tvnbkFCQPn2YPcyiwntFL9_US8n-rOxvbZIYoQ3wz8CFaRc3Jbi59Kpw.

[3] G. Martin, L. Rentsch, M. Höck, M. Bertau, Lithium market research – global supply, future demand and price development, Energy Storage Mater. 6 (2017) 171–179, https://doi.org/10.1016/j.ensm.2016.11.004.

[4] B.W. Jaskula, Mineral commodity summaries lithium, U.S. Geological Survey, Reston, VA, 2019, pp 98-99. https://prd-wret.s3-us-west-2.amazonaws.com/assets/palladium/production/atoms/files/mcs-2019-lithi.pdf.

[5] J. Speirs, M. Contestabile, Y. Houari, R. Gross, The future of lithium availability for electric vehicle batteries, Renew. Sustain. Energy Rev. 35 (2014) 183–193, https://doi.org/10.1016/j.rser.2014.04.018.

[6] U.S. Geological Survey, Mineral Commodity Summaries 2019, Mineral Commodity Summaries. (2019). https://doi.org/10.3133/70202434.

[7] Y. Jang, E. Chung, Adsorption of lithium from shale gas produced water using titanium based adsorbent, Ind. Eng. Chem. Res. 57 (25) (2018) 8381–8387, https://doi.org/10.1021/acs.iecr.8b0080510.1021/acs.iecr.8b00805.s001.

[8] E. Jang, Y. Jang, E. Chung, Lithium recovery from shale gas produced water using solvent extraction, Appl. Geochem. 78 (2017) 343–350, https://doi.org/10.1016/j.apgeochem.2017.01.016.

[9] Y. He, S.L. Flynn, E.J. Folkerts, Y. Zhang, D. Ruan, D.S. Alessi, J.W. Martin, G.G. Goss, Chemical and toxicological characterizations of hydraulic fracturing flowback and produced water, Water Res. 114 (2017) 78–87, https://doi.org/10.1016/j.watres.2017.02.027.

[10] R. Barati, J.-T. Liang, A review of fracturing fluid systems used for hydraulic fracturing of oil and gas wells, J. Appl. Polym. Sci. 131 (16) (2014) n/a-n/a, https://doi.org/10.1002/app.40735.

[11] D.L. Shaffer, L.H. Arias Chavez, M. Ben-Sasson, S. Romero-Vargas Castrillón, N.Y. Yip, M. Elimelech, Desalination and reuse of high-salinity shale gas produced water: drivers, technologies, and future directions, Environ. Sci. Technol. 47 (17) (2013) 9569–9583, https://doi.org/10.1021/es401966e.

[12] V. Flexer, C.F. Baspineiro, C.I. Galli, Lithium recovery from brines: a vital raw material for green energies with a potential environmental impact in its mining and processing, Sci. Total Environ. 639 (2018) 1188–1204, https://doi.org/10.1016/j.scitotenv.2018.05.223.

[13] T. Hano, M. Matsumoto, T. Ohtake, N. Egashir, F. Hori, Recovery of lithium from geothermal water by solvent extraction technique, Solvent Extr. Ion Exch. 10 (2) (1992) 195–206, https://doi.org/10.1080/07366299208918100.

[14] H. Kanoh, K. Ooi, Y. Miyai, S. Katoh, Electrochemical recovery of lithium ions in the aqueous phase, Sep. Sci. Technol. 28 (1–3) (1993) 643–651, https://doi.org/10.1080/01496399308019512.

[15] S. Safari, B.G. Lottermoser, D.S. Alessi, Metal oxide sorbents for the sustainable recovery of lithium from unconventional resources, Appl. Mater. Today 19 (2020) 100638, https://doi.org/10.1016/j.apmt.2020.100638.

[16] H. Lin, X. Yu, M. Li, J. Duo, Y. Guo, T. Deng, Synthesis of polyporous ion-sieve and its application for selective recovery of lithium from geothermal water, ACS Appl. Mater. Interfaces. 11 (29) (2019) 26364–26372, https://doi.org/10.1021/acsami.9b0740110.1021/acsami.9b07401.s001.

[17] Z.-Y. Ji, M.-Y. Zhao, J.-S. Yuan, J. Wang, J.-Q. Zhou, H.-B. Yin, B.-Y. Sun, Li + extraction from spinel-type LiMn2O4 in different eluents and Li + insertion in the aqueous phase, Solvent Extr. Ion Exch. 34 (6) (2016) 549–557, https://doi.org/10.1080/07366299.2016.1221266.

[18] P. Meshram, B.D. Pandey, T.R. Mankhand, Extraction of lithium from primary and secondary sources by pre-treatment, leaching and separation: a comprehensive review, Hydrometallurgy 150 (2014) 192–208, https://doi.org/10.1016/j.hydromet.2014.10.012.

[19] B. Swain, Recovery and recycling of lithium: a review, Sep. Purif. Technol. 172 (2017) 388–403, https://doi.org/10.1016/j.seppur.2016.08.031.

[20] C. Zhong, J. Li, S.L. Flynn, C.L. Nesbø, C. Sun, K. von Gunten, B.D. Lanoil, G.G. Goss, J.W. Martin, D.S. Alessi, Temporal changes in microbial community composition and geochemistry in flowback and produced water from the duvernay formation, ACS Earth Space Chem. 3 (6) (2019) 1047–1057, https://doi.org/10.1021/acsearthspacechem.9b0003710.1021/acsearthspacechem.9b00037.s001.

[21] L. Tian, W. Ma, M. Han, Adsorption behavior of Li + onto nano-lithium ion sieve from hybrid magnesium/lithium manganese oxide, Chem. Eng. J. 156 (1) (2010) 134–140, https://doi.org/10.1016/j.cej.2009.10.008.

[22] D.S. Freeman, W.G. Chapman, An improved oxalate method for the determination of active oxygen in manganese dioxide, Analyst. 96 (1971) 865–869, https://doi.org/10.1039/AN9719600865.

[23] Q. Feng, Y. Miyai, H. Kanoh, K. Ooi, Lithium(1) extraction/insertion with spinel-type lithium manganese oxides Characterization of redox-type and ion-exchange-type sites, Langmuir. 8 (7) (1992) 1861–1867, https://doi.org/10.1021/la00043a029.

[24] K. Ooi, Y. Miyai, J. Sakakihara, Mechanism of lithium(1) insertion in spinel-type manganese oxide Redox and ion-exchange reactions, Langmuir. 7 (6) (1991) 1167–1171, https://doi.org/10.1021/la00054a025.

[25] R.A. House, U. Maitra, L. Jin, J.G. Lozano, J.W. Somerville, N.H. Rees, A.J. Naylor, L.C. Duda, F. Massel, A.V. Chadwick, S. Ramos, D.M. Pickup, D.E. McNally, X. Lu, T. Schmitt, M.R. Roberts, P.G. Bruce, What triggers oxygen loss in oxygen redox cathode materials?, Chem. Mater. 31 (9) (2019) 3293–3300, https://doi.org/10.1021/acs.chemmater.9b0022710.1021/acs.chemmater.9b00227.s001.

[26] L.K. McLeod, G.H. Spikes, R.J. Kashtiban, M. Walker, A.V. Chadwick, J.D.B. Sharman, R.I. Walton, Structures of mixed manganese ruthenium oxides (Mn1-xRux)O2 crystallised under acidic hydrothermal conditions, Dalton Trans. 49 (8) (2020) 2661–2670, https://doi.org/10.1039/C9DT04156G.

[27] B. Ravel, M. Newville, Athena, artemis, hephaestus: data analysis for X-ray absorption spectroscopy usingIFEFFIT, J. Syn. Radiation. 12 (4) (2005) 537–541, https://doi.org/10.1107/S0909049505012719.

[28] J.M. Cerrato, M.F. Hochella, W.R. Knocke, A.M. Dietrich, T.F. Cromer, Use of XPS to identify the oxidation state of Mn in solid surfaces of filtration media oxide samples from drinking water treatment plants, Environ. Sci. Technol. 44 (15) (2010) 5881–5886, https://doi.org/10.1021/es100547q.

[29] X. Xu, Y. Chen, P. Wan, K. Gasem, K. Wang, T. He, H. Adidharma, M. Fan, Extraction of lithium with functionalized lithium ion-sieves, Prog. Mater Sci. 84 (2016) 276–313, https://doi.org/10.1016/j.pmatsci.2016.09.004.

[30] R. Chitrakar, H. Kanoh, Y. Miyai, K. Ooi, Recovery of lithium from seawater using manganese oxide adsorbent (H1.6Mn1.6O4) derived from Li1.6Mn1.6O4, Ind. Eng. Chem. Res. 40 (9) (2001) 2054–2058, https://doi.org/10.1021/ie000911h.

[31] K. Ooi, Y. Miyai, S. Katoh, Recovery of lithium from seawater by manganese oxide adsorbent, Sep. Sci. Technol. 21 (8) (1986) 755–766, https://doi.org/10.1080/01496398608056148.

[32] Q. Feng, H. Kanoh, Y. Miyai, K. Ooi, Hydrothermal synthesis of lithium and sodium manganese oxides and their metal ion extraction/insertion reactions, Chem. Mater. 7 (6) (1995) 1226–1232, https://doi.org/10.1021/cm00054a024.

[33] K. Sato, D.M. Poojary, A. Clearfield, M. Kohno, Y. Inoue, The surface structure of the proton-exchanged lithium manganese oxide spinels and their lithium-ion sieve properties, J. Solid State Chem. 131 (1) (1997) 84–93, https://doi.org/10.1006/jssc.1997.7348.

[34] L. Wang, W. Ma, R. Liu, H. Li, C. Meng, Correlation between Li adsorption capacity and the preparation conditions of spinel lithium manganese precursor, Solid State Ion. 177 (17–18) (2006) 1421–1428, https://doi.org/10.1016/j.ssi.2006.07.019.

[35] Q. Feng, H. Kanoh, K. Ooi, Manganese oxide porous crystals, J. Mater. Chem. 9 (1999) 319–333, https://doi.org/10.1039/a805369c.

[36] B. Ammundsen, P.. Aitchison, G.. Burns, D.. Jones, J. Rozière, Proton insertion and lithium-proton exchange in spinel lithium manganates, Solid State Ionics 97 (1–4) (1997) 269–276, https://doi.org/10.1016/S0167-2738(97)00065-9.

[37] R. Chitrakar, H. Kanoh, Y. Miyai, K. Ooi, A new type of manganese oxide (MnO2·0.5H2O) derived from Li1.6Mn1.6O4and its lithium ion-sieve properties, Chem. Mater. 12 (10) (2000) 3151–3157, https://doi.org/10.1021/cm0000191.

[38] P. Euzen, P. Leone, P. Palvadeau, M. Queignec, J. Rouxel, Synthesis and structural studies of manganese oxyhalides with a multisite framework, Mater. Res. Bull. 27 (11) (1992) 1295–1300, https://doi.org/10.1016/0025-5408(92)90094-G.

[39] P. Aitchison, B. Ammundsen, J. Rozière, G.R. Burns, D.J. Jones, Local structure and lithium-proton ion exchange in Li1.33−x/3CoxMn1.67−2x/3O4 spinels, Solid State Ionics 176 (7–8) (2005) 813–821, https://doi.org/10.1016/j.ssi.2004.10.009.

[40] B. Ammundsen, D.J. Jones, J. Rozière, G.R. Burns, Effect of chemical extraction of lithium on the local structure of spinel lithium manganese oxides determined by X-ray absorption spectroscopy, Chem. Mater. 8 (12) (1996) 2799–2808, https://doi.

org/10.1021/cm960287s.
[41] M.J. Ariza, D.J. Jones, J. Rozière, R. Chitrakar, K. Ooi, Probing the local structure and the role of protons in lithium sorption processes of a new lithium-rich manganese oxide, Chem. Mater. 18 (7) (2006) 1885–1890, https://doi.org/10.1021/cm052214r.
[42] W. Tang, H. Kanoh, X. Yang, K. Ooi, Preparation of plate-form manganese oxide by selective lithium extraction from monoclinic li2mno3under hydrothermal conditions, Chem. Mater. 12 (11) (2000) 3271–3279, https://doi.org/10.1021/cm000360l.
[43] Y. Li, Y. Bian, H. Qin, Y. Zhang, Z. Bian, Photocatalytic reduction behavior of hexavalent chromium on hydroxyl modified titanium dioxide, Appl. Catal. B 206 (2017) 293–299, https://doi.org/10.1016/j.apcatb.2017.01.044.
[44] A. Krauklis, R. Ozola, J. Burlakovs, K. Rugele, K. Kirillov, A. Trubaca-Boginska, K. Rubenis, V. Stepanova, M. Klavins, Klavins, FeOOH and Mn8O10Cl3modified zeolites for As(V) removal in aqueous medium, J. Chem. Technol. Biotechnol. 92 (8) (2017) 1948–1960, https://doi.org/10.1002/jctb.2017.92.issue-810.1002/jctb.5283.
[45] E. Halevas, A. Malakopoulos, A. Delimitis, V. Zaspalis, G. Litsardakis, A. Salifoglou, Manganese oxychloride-modified hydrophobic silica targets removal of nitrates from water, Water Air Soil Pollut. 224 (6) (2013), https://doi.org/10.1007/s11270-013-1598-x.
[46] E.V. Saenko, G.V. Leont'eva, V.V. Vol'khin, A.S. Kolyshkin, Variation of the composition and properties of lithium manganese oxide spinel in lithiation-delithiation cycles, Russ. J. Inorg. Chem. 52 (8) (2007) 1312–1316, https://doi.org/10.1134/S0036023607080256.
[47] K. Ooi, Y. Miyai, S. Katoh, H. Maeda, M. Abe, Lithium-ion insertion/extraction reaction with λ-MnO2in the aqueous phase, Chem. Lett. 17 (6) (1988) 989–992, https://doi.org/10.1246/cl.1988.989.
[48] J. Xiao, X. Nie, S. Sun, X. Song, P. Li, J. Yu, Lithium ion adsorption–desorption properties on spinel Li4Mn5O12 and pH-dependent ion-exchange model, Adv. Powder Technol. 26 (2) (2015) 589–594, https://doi.org/10.1016/j.apt.2015.01.008.
[49] A. Gao, Z. Sun, S. Li, X. Hou, H. Li, Q. Wu, X. Xi, The mechanism of manganese dissolution on Li1.6Mn1.6O4 ion sieves with HCl, Dalton Trans. 47 (11) (2018) 3864–3871, https://doi.org/10.1039/C8DT00033F.
[50] Y. Jang, E. Chung, Influence of alkanes on lithium adsorption and desorption of a H2TiO3 ion sieve adsorbent in synthetic shale gas-produced water, Ind. Eng. Chem. Res. 58 (48) (2019) 21897–21903, https://doi.org/10.1021/acs.iecr.9b0447210.1021/acs.iecr.9b04472.s001.
[51] Y. Jang, E. Chung, Lithium adsorptive properties of H2TiO3 adsorbent from shale gas produced water containing organic compounds, Chemosphere 221 (2019) 75–80, https://doi.org/10.1016/j.chemosphere.2019.01.032.
[52] A.T. Stone, J.J. Morgan, Reduction and dissolution of manganese(III) and manganese(IV) oxides by organics: 2 Survey of the reactivity of organics, Environ. Sci. Tech. 18 (8) (1984) 617–624, https://doi.org/10.1021/es00126a010.
[53] D.E. Canfield, B. Thamdrup, J.W. Hansen, The anaerobic degradation of organic matter in Danish coastal sediments: Iron reduction, manganese reduction, and sulfate reduction, Geochim. Cosmochim. Acta 57 (16) (1993) 3867–3883, https://doi.org/10.1016/0016-7037(93)90340-3.
[54] A.T. Stone, J.J. Morgan, Reduction and dissolution of manganese(III) and manganese(IV) oxides by organics. 1. Reaction with hydroquinone, Environ. Sci. Technol. 18 (6) (1984) 450–456, https://doi.org/10.1021/es00124a011.
[55] P.. Okita, J.B. Maynard, E.. Spiker, E.. Force, Isotopic evidence for organic matter oxidation by manganese reduction in the formation of stratiform manganese carbonate ore, Geochim. Cosmochim. Acta 52 (11) (1988) 2679–2685, https://doi.org/10.1016/0016-7037(88)90036-1.
[56] D.J. Burdige, The biogeochemistry of manganese and iron reduction in marine sediments, Earth Sci. Rev. 35 (3) (1993) 249–284, https://doi.org/10.1016/0012-8252(93)90040-E.
[57] W.G. Sunda, S.A. Huntsman, G.R. Harvey, Photoreduction of manganese oxides in seawater and its geochemical and biological implications, Nature 301 (5897) (1983) 234–236, https://doi.org/10.1038/301234a0.
[58] W.G. Sunda, S.A. Huntsman, Photoreduction of manganese oxides in seawater, Mar. Chem. 46 (1–2) (1994) 133–152, https://doi.org/10.1016/0304-4203(94)90051-5.
[59] D.A. Crerar, C. DA, C. RK, B. HL, Organic controls on the sedimentary geochemistry of manganese, Acta Mineral.-Petrogr. 20 (1971) 217-226.
[60] M.E. Ersahin, H. Ozgun, R. Kaya, B. Kose Mutlu, C. Kinaci, I. Koyuncu, Treatment of produced water originated from oil and gas production wells: a pilot study and cost analysis, Environ. Sci. Pollut. Res. 25 (7) (2018) 6398–6406, https://doi.org/10.1007/s11356-017-0961-7.
[61] Electric Power Monthly - U.S. Energy Information Administration (EIA). (2021). https://www.eia.gov/electricity/monthly/epm_table_grapher.php?t=epmt_5_6_a (accessed May 18, 2021).